Makara Journal of Technology

Volume 25 | Number 2 Article 3

8-2-2021

Effect of Arc Plasma Sintering on the Structural and Microstructural Properties of Fe-Cr-Ni Austenitic Stainless Steels

Parikin Parikin
Center for Science and Technology of Advanced Materials, National Nuclear Energy Agency (BATAN), South Tangerang 15314, Indonesia, farihin@batan.go.id

M. Dani
Center for Science and Technology of Advanced Materials, National Nuclear Energy Agency (BATAN), South Tangerang 15314, Indonesia

A. Dimyati
Center for Science and Technology of Advanced Materials, National Nuclear Energy Agency (BATAN), South Tangerang 15314, Indonesia

N. D. Purnamasari
Physics Department, Faculty of Natural Sciences, Institut Teknologi Sepuluh Nopember, Surabaya 60111, Indonesia

B. Sugeng
Physics Department, Faculty of Natural Sciences, Institut Teknologi Sepuluh Nopember, Surabaya 60111, Indonesia

Recommended Citation

Parikin, Parikin; Dani, M.; Dimyati, A.; Purnamasari, N. D.; Sugeng, B.; Panitra, M.; Insani, A.; Priyanto, T. H.; Mustofa, S.; Syahbuddin, Syahbuddin; and Huang, A. (2021) "Effect of Arc Plasma Sintering on the Structural and Microstructural Properties of Fe-Cr-Ni Austenitic Stainless Steels," *Makara Journal of Technology*: Vol. 25 : No. 2 , Article 3.
DOI: 10.7454/mst.v25i2.3922
Available at: https://scholarhub.ui.ac.id/mjt/vol25/iss2/3

Effect of Arc Plasma Sintering on the Structural and Microstructural Properties of Fe-Cr-Ni Austenitic Stainless Steels

Authors

Parikin Parikin, M. Dani, A. Dimyati, N. D. Purnamasari, B. Sugeng, M. Panitra, A. Insani, T. H. Priyanto, S. Mustofa, Syahbuddin Syahbuddin, and A. Huang

Makara J. Technol. 25/2 (2021), 71–78
doi: 10.7454/mst.v25i2.3922

Effect of Arc Plasma Sintering on the Structural and Microstructural Properties of Fe-Cr-Ni Austenitic Stainless Steels

Parikin[1*], M. Dani[1], A. Dimyati[1], N. D. Purnamasari[2], B. Sugeng[1], M. Panitra[1], A. Insani[1], T.H. Priyanto[1], S. Mustofa[1], Syahbuddin[3], and C. A. Huang[4]

1. Center for Science and Technology of Advanced Materials, National Nuclear Energy Agency (BATAN), South Tangerang 15314, Indonesia
2. Physics Department, Faculty of Natural Sciences, Institut Teknologi Sepuluh Nopember, Surabaya 60111, Indonesia
3. Department of Mechanical Engineering, Faculty of Engineering, University of Pancasila, Jakarta 12640, Indonesia
4. Department of Mechanical Engineering, Chang Gung University, Taoyuan City 33302, Taiwan

[*]*E-mail: farihin@batan.go.id*

Abstract

X-ray diffraction techniques were performed to determine the actual crystal structure of A2 austenitic stainless steel (ASS) as-cast and A2 ASS after arc plasma sintering (APS) for 2 s. Computations were conducted on the basis of the Bragg arithmetic formula by comparing the S^2 arithmetic with the interplanar spacing. The Bragg arithmetic formula is a simple series for the determination of the crystalline phase of materials based on the Miller indices of cubic shapes or other shapes. A2 ASS as-cast was identified to have a crystal structure of face-centered cubic with lattice parameter a = 3.58 Å. A similar crystal structure can still be detected in A2 ASS after APS for 2 s with lattice parameter a = 3.60 Å. This finding was confirmed by neutron diffraction measurements and optical–electron microscopy observations. Under the same conditions, both A2 ASS as-cast and A2 ASS after APS for 2 s have similar cast structures. The grain boundary formed in A2 ASS as-cast is thinner than that in A2 ASS after APS for 2 s, which is visible in its boundaries. Moreover, the grain structure of A2 ASS after APS for 2 s, which was originally elongated particles, became globular particles. Similarly, granular precipitates became concentrated and encompassed the steel matrix along the grain boundaries. Furthermore, scanning electron microscopy with energy-dispersive X-ray analysis showed that particles and islands in steel are distributed in the grains and at the grain boundaries, respectively. Precipitates are composed of C, Cr, Fe, and Ni. The elemental contents of Cr and C are dominant; thus, Cr23C6 precipitate is formed at the grain boundaries.

Abstrak

Pengaruh Sintering *Arc-Plasma* pada Sifat Mikro dan Struktur Baja Tahan Karat Austenitik Fe-Cr-Ni. Dalam penelitian ini, teknik difraksi sinar-X dilakukan untuk mengetahui bentuk struktur kristal dan parameter kisi sebenarnya baja nirkarat austenitik (ASS) A2 *as-cast* dan A2-ASS yang disinter plasma selama 2 detik. Perhitungan dilakukan dengan menggunakan dasar rumus Bragg, dengan membandingkan nilai S-aritmatika dan jarak antarplanar. Aritmatika Bragg adalah rangkaian sederhana dari penentuan kristal suatu bahan berdasarkan bentuk kubik Indeks Miller atau lainnya. ASS teridentifikasi memiliki struktur kristal *face centered cubic* (FCC) dengan parameter kisi a = 3,58 Å. Struktur kristal yang serupa masih ditemukan di ASS setelah *arc plasma sintering* (APS) selama 2 detik dengan parameter kisi a = 3,60 Å. Hasilnya dikonfirmasi dengan pengukuran difraksi neutron dan pengamatan struktur mikro menggunakan Mikroskop Optik (MO) dan Elektron (SEM). Dengan asumsi kondisi yang sama saat proses pengecoran, kedua ASS A2 memiliki struktur cor yang sama, batas butir yang dibentuk dalam ASS A2 *as-cast* lebih tipis daripada batas butir dalam ASS A2 setelah APS selama 2 detik yang cenderung sangat terlihat sangat jelas batas-batasnya. Sementara, pola butiran dalam A2 ASS setelah APS selama 2 detik, partikel yang awalnya memanjang berubah menjadi partikel globular pada struktur butir. Demikian juga, endapan granular sangat terkonsentrasi melingkupi butiran matriks baja di sepanjang batas butir. Pengamatan SEM-EDX menunjukkan bahwa precipitat *islands* dan *particles* di kedua ASS A2 berturutan tersebar di batas butir dan di butir. Komposisi presipitat dalam A2 ASS adalah C, Cr, Fe dan Ni. Kandungan unsur Cr dan C sangat dominan sehingga presipitat Cr23C6 sudah terbentuk pada batas butir.

Keywords: A2 austenitic stainless steel, arc plasma sintering, Bragg arithmetic, neutron diffraction, optical–electron microscope, XRD

1. Introduction

Steel is an iron alloy with several other elements, including carbon as the main additive element. The carbon content in steel ranges from 0.2% to 2.1% [1]. The following elements are always present in the composition of steel: manganese, phosphorus, sulfur, silicon, and a small portion of oxygen, nitrogen, and aluminum. Moreover, other elements, including nickel, chrome, molybdenum, boron, titanium, vanadium, and niobium, are added to distinguish the characteristics of several types of steel. By varying the contents of carbon and other elements, various types of quality steel alloy can be synthesized into superalloy steel. As has been done by material engineers in BATAN since 2006 [2], synthesis of serial austenitic stainless steel (ASS) and ferritic stainless steel for high-temperature structural materials has been conducted to generate components for nuclear reactors. Steels defined as alloyed metal show some extreme characteristics, such as high mechanical strength and excellent corrosion/oxidation resistance. Previous research reported excellent mechanical properties, such as formability with the cold rolling process, weldability, and residual stress [3]. The average hardness of this material is approximately 160 HVN (84 HRC). A recent study reported that this type of steel showed good corrosion rates, i.e., approximately 0.088 mm/year [4], and was resistant to oxidation at 850 °C [5]. One of these characteristics can be influenced by the formation of the crystal structure.

The performance of the material can be continuously increased by applying arc plasma sintering (APS) [6] treatments to improve the performance of the microstructure and minimize the porosity of the material. This sintering process involves the compaction and formation of a solid mass of material heated without melting it to the point of liquefaction.

To determine the crystal structure of steel, diffraction techniques, including X-ray diffraction (XRD), can be used. The results of XRD measurements include a diffraction profile, which is a characteristic pattern of a material that is different from one to another. Notably, if X-rays strike the surface of a material, then it will exhibit some optical phenomena, such as diffraction, transmission, and reflection. When X-rays strike the crystal planes, X-rays will be diffracted from a specific angle. The diffraction pattern displays an angular measurement in the form of scattering angle (2θ) and diffraction intensity (I). The pattern between scattering angle and diffraction intensity is the embodiment of Bragg's Law, which can be used to predict the crystal structure and lattice parameters of the material.

Thus, this article simply describes the determination of the crystal structure and the calculation of the lattice parameters from the diffraction profile through the equation expressing their relationship on the reflection plane, where *hkl* (Miller indices) is an arithmetic series with the interplanar distance *d*. The microstructures of both samples are also discussed and compared with each other so that the APS effects can be further observed.

2. Bragg Arithmetic Formula

XRD is an analytical method used to identify the crystalline phase in the material by determining the lattice parameters of the structure and the particle size. The output of a diffraction device is a profile known as a diffraction pattern that can provide qualitative and semiquantitative data on solid samples. XRD techniques can be used to measure the average distance between atomic layers, determine the single and polycrystalline structures of unknown materials, and measure the shape, size, and stress of small crystals [7]. This technique is based on a monochromatic X-ray that deals with crystalline material so that each crystal plane will reflect or scatter X-rays in all directions (isotropic). Interference occurs only between reflected rays in phase. Mutually reinforcing interference occurs only if the X-ray that has the phase has different multiples of integers of wavelengths. This statement is called Bragg's Law for crystal diffraction [8].

Bragg's Law is generally formulated as expressed in Equation (1):

$$n\lambda = 2\, d_{hkl} \sin \theta_{hkl} \tag{1}$$

or

$$d_{hkl} = \lambda/(2 \sin \theta_{hkl}) \tag{2}$$

where $n = 1$. By inputting the wavelength of the Cu target (λ_{Cu}) value of 1.54 Å, the distance between the planes of the diffraction peak d_{hkl} can be obtained. Furthermore, from the combination of the d_{hkl} values of a cubic crystal structure, the lattice parameter a can be calculated using Equation (5) as a derivative of Equation (3), which is a form of arithmetic series of the Miller indices, and Equation (4) as follows:

$$S^2 = h^2 + k^2 + l^2, \tag{3}$$

$$(a/dhkl)^2 = (h^2 + k^2 + l^2). \tag{4}$$

Then, the following relationship can be obtained:

$$a = S \cdot d_{hkl}. \tag{5}$$

The S^2 arithmetic for simple crystal structures, such as simple cubic (SC), body-centered cubic (BCC), and face-centered cubic (FCC), are listed in Table 1.

Table 1. Miller Indices Arithmetic

Crystal Structure	*hkl* Plane	*S*2
SC—Simple Cubic	100, 110, 111, 200, 210, 211, 220, 221, …	1, 2, 3, 4, 5, 6, 8, 9, …
BCC—Body-Centered Cubic	110, 200, 211, 220, 310, 222, 400, …	2, 4, 6, 8, 10, 12, 16, …
FCC—Face-Centered Cubic	111, 200, 220, 311, 222, 400, 331, 420, …	3, 4, 8, 11, 12, 16, 19, 20, …

3. Experimental

The materials used in this study are A2 ASS as-cast and A2 ASS after APS for 2 s. A2 ASS is a nonstandard and low-carbon steel made by casting techniques using an induction furnace. The stainless steel ingots were synthesized at the Indonesian Institute of Sciences (LIPI), Bandung [9].

Characterization of the crystal structure, microstructure, and composition was conducted using optical microscopy, scanning electron microscopy with energy-dispersive X-ray analysis (SEM-EDX), XRD, and high-resolution powder neutron diffraction. The chemical composition of A2 ASS as-cast was measured using optical erosion spectroscopy, and the elements contained in A2 ASS as-cast are listed in Table 2.

The samples of A2 ASS as-cast and A2 ASS after APS for 2 s are shown in Figure 1. These samples were characterized by successive crystal structures using an X-ray diffractometer (Phillips PANalytical Empyrean PW1710) and a high-resolution powder neutron diffractometer. The microstructures of both samples were observed through an Olympus optical microscope and a Jeol SEM-EDX 2650LA at the Advanced Material Science and Technology Center (PSTBM), BATAN.

A beamformed material with a coupon with the dimension of 35 × 30 × 15 mm^3 was used to facilitate the placement of the samples on the table of the test equipment. Meanwhile, the measurement of the XRD pattern was done using a Cu target wavelength of 1.54 Å with a step count of 0.05° and scattering angle (2θ) ranging from 30° to 100°, with step and preset mode counts for 2 s. Meanwhile, the measurement of the neutron diffraction pattern was done with a neutron thermal wavelength of 1.82 Å. After going through the metal preparation process, the characterization of the samples was followed by microstructure observation using an optical microscope and an SEM-EDX to observe the differences in the microstructures of A2 ASS as-cast and A2 ASS after APS for 2 s.

Table 2. Chemical composition of A2 ASS as-cast

Element	wt%
Fe	Balance
Ni	25.04
Cr	16.55
Mn	0.504
Si	0.89
Al	0.003
Ti	0.004
Sn	0.01
C	0.293
P	0.13

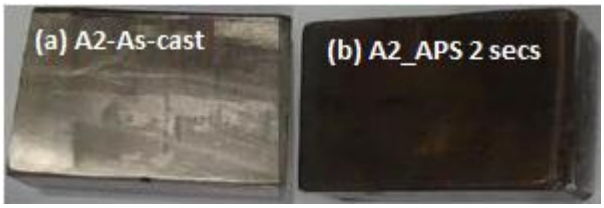

Figure 1. Samples of (a) A2 ASS as-cast and (b) A2 ASS after APS for 2 s

4. Results and Discussions

Diffraction evaluation. The measurement results of the diffraction patterns of the samples of A2 ASS as-cast and A2 ASS after APS for 2 s using XRD machines with Cu target wavelength are shown in Figure 2.

On the basis of the diffraction patterns, calculations are made to determine the crystal structure and lattice parameter (*a*, *b*, *c*) of each sample by determining the 2θ value of each peak in the pattern and the sin θ. Furthermore, by inputting λ = 1.54 Å to Equation (2), the *dhkl* value is obtained as the value of d1, d2, and d3. The data obtained are listed in Table 3 and Table 4.

To determine the crystal structure and lattice parameters of each sample, Equation (5) can be used. The description of the arithmetic tabulations are listed in Table 5 and Table 6.

The results tabulated in Table 5 show that the A2 ASS as-cast sample has an arithmetic series of 3, 4, 8, 11, 12, … (see values highlighted in green and rendered in bold), which is equivalent to the plane of (111), (200), (220), (311), (222), …. According to the data shown in Table 1, the crystal structure of A2 ASS as-cast is FCC, with a mean lattice parameter value of approximately 3.58 Å.

A similar method is utilized for A2 ASS after APS for 2 s, and its results are tabulated in Table 6, where the sample has an arithmetic series of 3, 4, 8, 11, 12, … (see values highlighted in blue and rendered in bold), which is equivalent to the plane of (111), (200), (220), (311), (222), …. According to the data shown in Table 1, the crystal structure of A2 ASS after APS for 2 s is also FCC with a mean lattice parameter value of 3.60 Å. The lattice of A2 ASS after APS for 2 s is slightly larger than that of A2 ASS as-cast.

Table 3. dhkl Calculation Results of A2 ASS as-cast

2*θ*/°	*θ*/°	sin *θ*	*d*/Å	*di*
43.62268	21.81134	0.371694	2.072135	*d1*
50.68294	25.34147	0.428173	1.798806	*d2*
74.79761	37.39881	0.607568	1.267677	*d3*
90.88183	45.44091	0.712751	1.080601	*d4*
96.25888	48.12944	0.744880	1.033992	*d5*

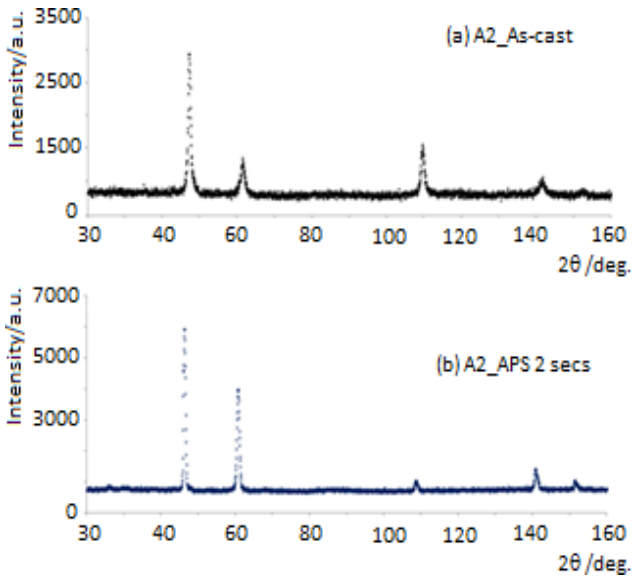

Figure 2. X-ray Diffraction (XRD) Profiles for Samples of (a) A2 ASS as-cast and (b) A2 ASS after APS for 2 s

Table 4. *dhkl* Calculation Results of A2 ASS after APS for 2 s

2*θ*/°	*θ*/°	sin *θ*	*d*/Å	*di*
43.10645	21.55323	0.367506	2.095747	*d1*
50.35437	25.17718	0.425579	1.809770	*d2*
74.33026	37.16513	0.604322	1.274485	*d3*
90.42799	45.21400	0.709967	1.084840	*d4*
96.70636	47.85318	0.741653	1.038491	*d5*

Table 5. S^2 Arithmetic and *dhkl* Values of A2 ASS as-cast

TER

hkl	S^2	S	d_1	d_2	d_3	d_4	d_5
			2.072135	1.798806	1.267677	1.080601	1.033992
100	1	1	2.072135	1.798806	1.267677	1.080601	1.033992
110	2	1.414214	2.930441	2.543896	1.792766	1.528201	1.462286
111	3	1.732051	3.589043	3.115623	2.195681	1.871656	1.790927
200	4	2	4.144270	3.597612	2.535354	2.161202	2.067984
210	5	2.236068	4.633435	4.022252	2.834612	2.416297	2.312076
211	6	2.44949	5.075673	4.406157	3.105162	2.646921	2.532753
	7	2.645751	5.482354	4.759193	3.353958	2.859002	2.735686
220	8	2.828427	5.860883	5.087792	3.585532	3.056401	2.924571
300	9	3	6.216405	5.396418	3.803031	3.241803	3.101976
310	10	3.162278	6.552666	5.688324	4.008747	3.417160	3.269770
311	11	3.316625	6.872494	5.965965	4.204409	3.583948	3.429364
222	12	3.464102	7.178086	6.231247	4.391362	3.743312	3.581853

Table 6. S^2 Arithmetic and *dhkl* Values of A2 ASS after APS for 2 s

hkl	S^2	S	d_1	d_2	d_3	d_4	d_5
			2.095747	1.80977	1.274485	1.088484	1.038491
100	1	1	2.095747	1.80977	1.274485	1.088484	1.038491
110	2	1.414214	2.963834	2.559401	1.802394	1.539549	1.468648
111	3	1.732051	3.62994	3.134614	2.207473	1.88531	1.798719
200	4	2	4.191494	3.61954	2.54897	2.176968	2.076982
210	5	2.236068	4.686233	4.046769	2.848835	2.433924	2.322136
211	6	2.44949	5.133511	4.433013	3.121838	2.66623	2.543773
	7	2.645751	5.544825	4.788201	3.37197	2.879858	2.747589
220	8	2.828427	5.927668	5.118803	3.604788	3.078698	2.937296
300	9	3	6.287241	5.42951	3.823455	3.265452	3.115473
310	10	3.162278	6.627334	5.722995	4.030275	3.442089	3.283997
311	11	3.316625	6.950806	6.002328	4.226989	3.610093	3.444285
222	12	3.464102	7.259881	6.269227	4.414946	3.770619	3.597438

Figure 3 shows the XRD pattern of the material that has been successfully identified by constructing its crystal structure with the Miller reflection/index plane shown as the calculation result of the correlation between the Bragg arithmetic formula in Equation (1) and S^2 arithmetic series in Equation (3).

Figure 4 shows the comparison of the neutron diffraction pattern and XRD profile of the samples. The samples of A2 APS as-cast and A2 ASS after APS for 2 s were analyzed using the MAUD software made by Lutterotti [10]. The samples were measured with a neutron thermal wavelength of 1.82 Å at the G.A. Siwabessy BATAN reactor in Serpong.

The refinements shown in Figure 4 indicate that the structure is an FCC (γ-Fe) crystal system. The diffraction peaks denote the reflection planes of (111), (200), (220), (311), and (222), which are patterned as all

even or odd numbers. There is no evidence of any other phase in all of the diffraction patterns detected in each zone. The results of the XRD measurements of the samples of A2 ASS as-cast and A2 ASS after APS for 2 s can be considered a measure of the total FCC with the lattice parameters of approximately 3.58 and 3.60 Å, respectively. The refinements were performed using single-phase models, i.e., the austenite phase (γ-Fe) with space group Fm3 m (I-225), and the results are listed in Table 7.

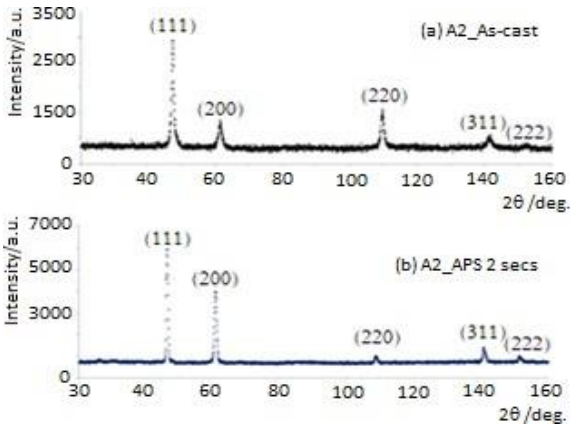

Figure 3. Identification of the XRD Profiles of the Samples of (a) A2 ASS as-cast and (c) A2 ASS after APS for 2 s using the Bragg Arithmetic Formula

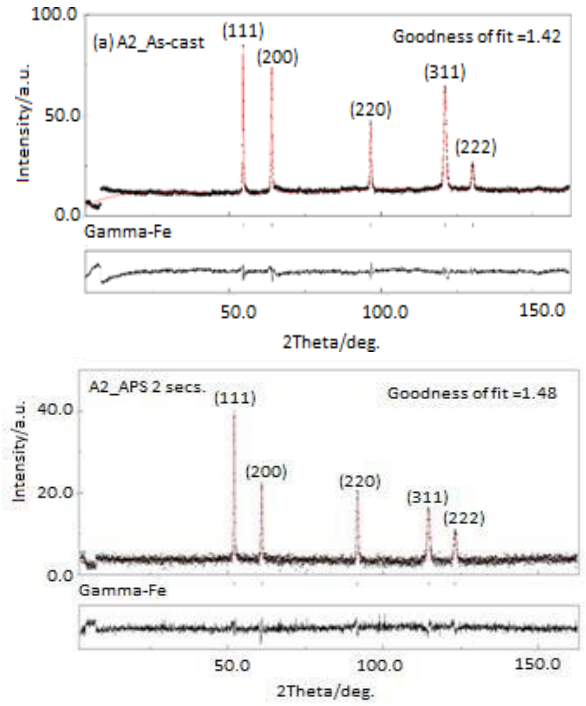

Figure 4. MAUD Refinements of the Neutron Diffraction Pattern of (a) A2 ASS as-cast and (b) A2 ASS after APS for 2 s through the Rietveld Method

Table 7. MAUD Refinement Parameters of the Crystal Structures of A2 ASS as-cast and A2 ASS After APS 2 s

Sample	*hkl* plane	2*θ*/°	*a*/Å	Goodness of fit, *S*
A2_As-cast	111	52.23	3.58(1)	1.42
	200	61.04		
	220	91.88		
	311	114.69		
	222	122.88		
A2_APS 2 s	111	51.94	3.60(3)	1.48
	200	60.75		
	220	91.30		
	311	113.98		
	222	122.30		

Microstructure. Using an optical microscope with 100× magnification, the microstructure of A2 ASS is observed, as shown in Figure 5. The homogeneous microstructures in A2 ASS show the characteristic of cast material, i.e., dendrite structures. Under the same casting process conditions, the cast structure of A2 ASS seems to be influenced by material sensitization to the cooling process [10], which produces a grain boundary that is thinner than the grain boundary in A2 ASS after APS for 2 s. The grain boundary tends to have clearly bounded limits (see Figure 5a and 5b). The ice flower pattern of the granules is noticeable on the microstructure of A2 ASS as-cast, which shows a needle-like [11] elongated and oriented overlapping and intertwining in the observation spot. In both A2 ASS as-cast and A2 ASS after APS for 2 s, precipitation formation occurs along the grain boundary. The precipitates grow along the observed grain boundary, and the number of precipitates is higher in A2 ASS after APS for 2 s than A2 ASS as-cast. However, for A2 ASS after APS for 2 s (Figure 5b), the elongated grain pattern seems to change to a globular structure. As a result of the sintering/heating process, the elongated granules melt and combine to form a larger colony. Similarly, the more concentrated worm-like precipitates cover the grains of the matrix.

Figure 6 shows the microstructure of A2 ASS as-cast observed through an electron microscope with 1,000× magnification (SEM-1,000×). Figure 5 shows that the precipitates on the microstructure of A2 ASS as-cast are distributed throughout the sample. The grains form longitudinal needles (islands) surrounding the particles (black dotted line), indicating that precipitates grow along the grain boundary. The distribution shows that A2 ASS as-cast has more precipitates than A2 ASS after APS for 2 s (see Figure 5a and 5b). Notably, steel is an alloy of Fe and C. In the austenitic phase, steel is only able to dissolve 2.14% carbon. Thus, if too many elements are incorporated into the composition of steel, it becomes saturated and forms precipitates [12].

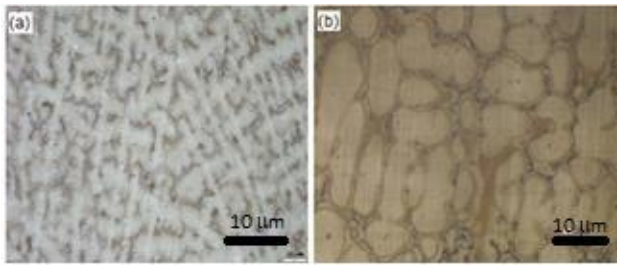

Figure 5. Optical Micrographs showing the Microstructures of (a) A2 ASS as-cast and (b) A2 ASS after APS for 2 s (100× Magnification)

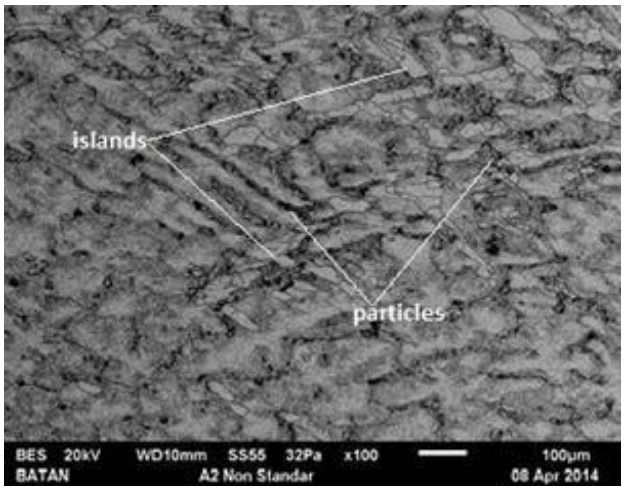

Figure 6. SEM Micrograph showing the Microstructure of A2 ASS as-cast (100× Magnification)

Under 100× magnification, no other phase is observed in the microstructure of A2 ASS as-cast. Thus, a homogeneous dendrite structure is observed in the entire sample, which is a characteristic of cast material. By contrast, under 1,000× magnification, the precipitates are observed to be distributed throughout the surface of the sample, with the grains elongated because of the influence of rolling (texturing). Texturing of the precipitates in the grain boundary occurs when 2 s APS is applied to A2 ASS. This comparison is confirmed by observing the microstructures of A2 ASS shown in Figure 5 and Figure 6.

Meanwhile, under 100× magnification, a homogeneous microstructure with no other phase is observed in A2 ASS with a fine dendritic shape in cast material. Under 100× magnification, the microstructure of A2 ASS shows precipitates confined along the grain boundary. More precipitates formed in A2 ASS as-cast than in A2 ASS after APS for 2 s. Furthermore, if the images shown in Figure 5a (OM-100×) and Figure 5b (OM-100×) are observed in detail, a noticeable difference is detected in A2 ASS after APS for 2 s, i.e., precipitation formation decreases.

EDX Spectrum. As shown in Figure 7, the microstructures of A2 ASS after APS for 2 s are generally composed of dendrites of γ-austenite as matrix and separated by the eutectic structure of Fe-Cr-C alloy. The dendrite arm spacing of A2 ASS as-cast is calculated to be approximately 223 µm. Most edges of the dendrite structure are filled with carbide particles. Meanwhile, the eutectic structure of Fe-Cr-C in grain boundaries consists of discontinuous carbide islands surrounded by γ-austenite zones, also known as particle-free zones. These carbide islands in A2 ASS as-cast as a part of the eutectic structure develop preferentially at the grain boundary [13]-[14].

Using EDX analysis, the composition of the island shown in Figure 6 is confirmed to have constituents close to the carbide of $(Cr,Fe)_{23}C_6$. The number of the eutectic structure at interdendrites decreases with the increase in sintering time. Moreover, the main part of interdendrites is detected in the thin boundary and only a few eutectic structures are observed after APS for 2 s. Meanwhile, in the same figure, the composition of particles is similar to the $(Cr,Fe)_7C_3$ carbide composition.

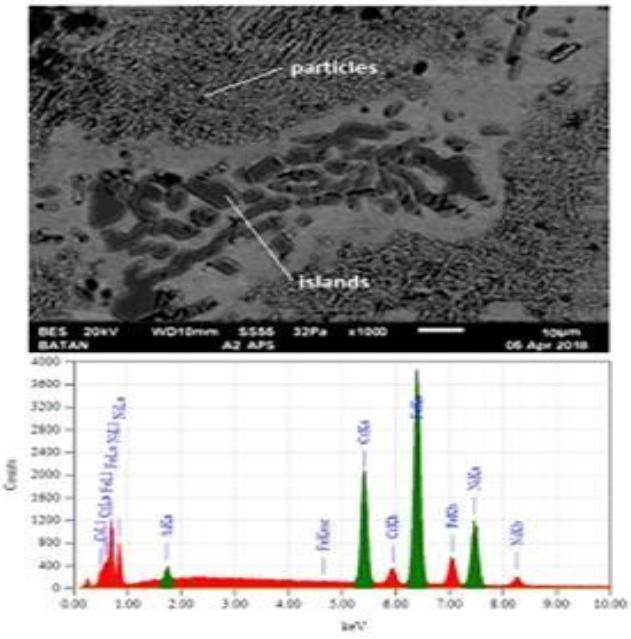

Elements	Mass %
Si	1.00
Cr	16.28
Fe	56.78
Ni	25.94
Total	100.00

Figure 7. SEM-1,000× Micrograph of the Microstructure of A2 ASS after APS for 2 s and its EDX Spectrum

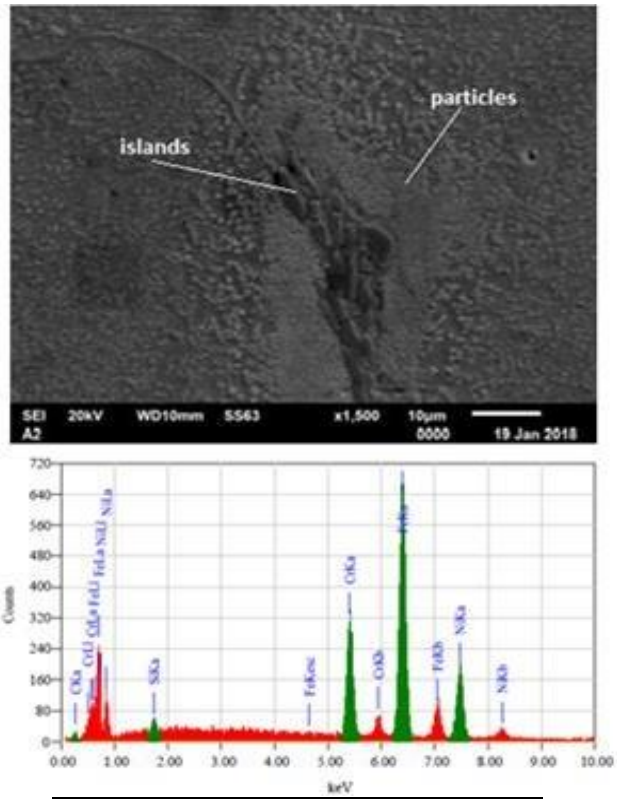

Elements	Mass %
C	2.61
Si	0.93
Cr	16.09
Fe	54.72
Ni	25.65
Total	100.00

Figure 8. SEM-1,500× Micrograph of the Microstructure of A2 ASS as-cast and its EDX Spectrum

Thus, such discontinuous carbide islands and particles in Fe-Cr-C alloys can be considered $(Cr,Fe)_{23}C_6$ and $(Cr,Fe)_7C_3$ carbide compositions, respectively. The islands of $(Cr,Fe)_{23}C_6$ in the eutectic structure tend to be smaller after APS for 2 s. By contrast, the sizes of the carbide particles of (Cr,Fe)7C3 in A2 ASS differ before and after sintering. Thus, the sintering time leads to the refinement of the $(Cr,Fe)_{23}C_6$ carbide islands in the eutectic structure but has no effect on the development of $(Cr,Fe)_7C_3$ particles at the edge of the dendrite matrix of A2 ASS.

SEM-EDX observation with 1,500× magnification to identify the spectrum of A2 ASS is shown in Figure 8. The semiquantitative chemical composition of the material measured in the material indicates that the dominant constituent elements in A2 ASS are C, Cr, Fe, and Ni. Elemental measurements further show that precipitation formation in both A2 ASS as-cast and A2 ASS after APS for 2 s occurs inside the grain boundary containing islands and particles. Because the dominant elements are Cr and C, the chrome carbide of $Cr_{23}C_6$ [15] forms as precipitate at the grain boundaries.

5. Conclusions

Calculations using the Bragg arithmetic formula show that A2 ASS as-cast has an FCC structure with lattice parameter a = 3.58 Å. The crystal structure formed in A2 ASS after APS for 2 s is identified to also have an FCC structure with lattice parameter a = 3.60 Å. Both of these measurements are confirmed to be the same as the results of neutron diffraction inspection. Under the same conditions of the casting process, both A2 ASS as-cast and A2 ASS after APS for 2 s have similar cast structures. The grain boundary formed in A2 ASS as-cast is thinner than the grain boundary formed in A2 ASS after APS for 2 s, which tends to be visible in its boundaries. Moreover, the grain structure of A2 ASS after APS for 2 s, which was originally elongated particles, became globular particles. Similarly, granular precipitates became concentrated and encompassed the steel matrix along the grain boundaries. SEM-EDX observation shows that precipitates in both A2 ASS as-cast and A2 ASS after APS for 2 s are distributed at the grain boundaries (islands) and in the grains (particles). Precipitates in A2 ASS are composed of C, Cr, Fe, and Ni. Because the dominant elements are Cr and C, the chrome carbide of $Cr_{23}C_6$ forms as precipitate at the grain boundaries.

Acknowledgments

The authors thank the head of PSTBM and BSBM, BATAN and also Mr. Sumaryo, Mr. Agus Sujatno, and Mr. Rohmad Salam for their kind help. In addition, the financial support of this study was funded by InSiNas 2019.

References

[1] W.D. Callister Jr., D.G. Rethwish, Materials Science and Engineering, SI Version, John Wiley & Sons, Inc, New York, U.S.A., 2011.
[2] N. Effendi, A.K. Jahja, B. Bandriyana, *et al*., Urania Sci. J. Nucl. Fuel Cycl. 18/1 (2012) 48.
[3] Parikin, Ismoyoi, R. Iskandar *et al*., Makara J. Tech. Univ. Indones. 21/2 (2017) 49.
[4] I. Wahyono, R. Salam, A. Dimyati *et al*., Pros. Sem. Nas. SDM Tek. Nuklir. (2015) 112.
[5] Parikin, B. Sugeng, M. Dani *et al*., Indones. J. Sci. Mat. 18/4 (2017) 179.
[6] A. Dimyati, B. Bandriyana, P. Untoro *et al*., Pros. Sem. Nas. Sains dan Tek. Nukl. BATAN Bandung. 14.

[7] Suharyana, Dasar-Dasar Dan Pemanfaatan Metode Difraksi Sinar-X, Universitas Sebelas Maret Surakarta, 2012.
[8] B.D. Cullity, S.R. Stock, Elements of X-Ray Diffraction 3rd ed., Pearson Ed. Lim., 2014.
[9] Parikin, N. Effendi, H. Mugihardjo *et al*., Urania, Sci. J. Nucl. Fuel Cycl. 20/1 (2014) 33.
[10] L. Lutterotti, MAUD tutorial-instrumental Broadening Determination, Dipartimento di Ingegneria dei Materiali, Universita di Trento 38050 Trento, Italy, 2006.
[11] Y. Handoyo, Jurnal Imiah Teknik Mesin, 3/2 (2015).
[12] Parikin, M. Dani, A.H. Ismoyo *et al*., Makara J. Tech. Univ. Indones. 22/2 (2018) 66.
[13] M. Dani, Parikin, R. Iskandar *et al*., J. Sci. Mat. Ind. 18/4 (2017) 173.